Interface engineering for substantial performance enhancement in epitaxial all-perovskite oxide capacitors

Jeongil Bang[1,2], Jaeho Lee[1], Eun Cheol Do[1], Hyungjun Kim[1], Byunghoon Na[1], Haeryong Kim[1], Bo-Eun Park[1], Jooho Lee[1], Che-Heung Kim[1], Ho Won Jang[2] and Yongsung Kim[1]

Abstract

Capacitors based on ABO_3-type perovskite oxides show considerable promise for overcoming the limitations of nanoscale integration with dynamic random access memory (DRAM) devices. Among the thermodynamically stable perovskite oxides, titanates ($ATiO_3$) exhibit high dielectric permittivity in metal–insulator–metal (MIM) configurations. However, their performance in mitigating the large leakage current caused by their narrow bandgap (3 eV) remain under scrutiny. Herein, substantially enhanced dielectric properties of an epitaxial $SrRuO_3/Ba_{0.5}Sr_{0.5}TiO_3/SrRuO_3$ MIM capacitor with a thin dielectric layer (10 nm) are reported. The dielectric/electrode heterointerface was engineered to realize a capacitor with a low leakage current and high dielectric permittivity. A pit-free and stoichiometric $SrRuO_3$ bottom electrode with an atomically smooth surface was exploited to suppress defect formation at the heterointerface. The critical roles of oxygen vacancies and substituted transition-metal atoms in determining the leakage current were assessed, and a strategy for reducing the leakage current via interface engineering was established. Consequently, a dielectric permittivity of 861 and a leakage current density of 5.15×10^{-6} A/cm^2 at 1 V were obtained with the thinnest dielectric layer ever reported. Our work paves the way for the development of perovskite-oxide-based capacitors in next-generation DRAM memories.

Introduction

Dynamic random access memory (DRAM) operation requires a certain level of charge-storage capacity. With developments in DRAM generation, the thickness of capacitors should decrease to satisfy the high-aspect-ratio requirement established by the design rule for DRAM capacitors. However, this scaling down of capacitors limits their charge-storage capability. Therefore, the properties of the thin dielectric layer must be enhanced and optimized[1,2].

To overcome these problems, investigations on metal–insulator–metal (MIM) capacitors must be

conducted to leverage their high dielectric permittivity (κ) values and thin dielectric layers. Because increasing the permittivity of the dielectric in an ultrathin capacitor can offset the aforementioned charge-storage limitations, ternary perovskite oxides that exhibit higher dielectric permittivity values than ZrO_2 and HfO_2, which are currently used in DRAM capacitors, have attracted research attention. In particular, $SrTiO_3$ and doped $SrTiO_3$ are representative ternary perovskite oxide materials; $SrTiO_3$ exhibits general dielectric characteristics, whereas Ba-doped $SrTiO_3$, a representative relaxor ferroelectric material, shows extremely high dielectric permittivity at the ferroelectric-to-paraelectric transition temperature. $SrTiO_3$ shows paraelectric properties and has no transition temperature, which shows a transition in dielectric properties. However, Ba-doped $SrTiO_3$ substituted with Ba instead

Correspondence: Ho Won Jang (hwjang@snu.ac.kr) or
Yongsung Kim (kimyongsung@samsung.com)
[1]Beyond Silicon Lab, Samsung Advanced Institute of Technology, Suwon 16678, South Korea
[2]Department of Materials Science and Engineering, Seoul National University, Seoul 08826, South Korea

of Sr at the A-sites of $SrTiO_3$ shows a ferroelectric-to-paraelectric transition. The transition temperature increases with increasing amounts of doped Ba. Therefore, a high dielectric permittivity can be achieved with Ba-doped $SrTiO_3$ at a desired temperature by controlling the Ba concentration[3–5].

In the dielectric layer, carriers can be transferred via two mechanisms: material-property-induced and defect-induced carrier conduction. Material property-induced carrier conduction includes Schottky emission and direct tunneling, which occur when the bandgap of the dielectric is narrow and when the dielectric is extremely thin, respectively. Defect-induced carrier conduction includes Poole–Frenkel (P–F) emission and hopping conduction, which are caused by defects acting as trap sites in the dielectric layer. Both mechanisms, which are caused by material properties and defects in the dielectric layer, affect the leakage current and are simultaneously activated. Therefore, as the thickness of $SrTiO_3$ or Ba-doped $SrTiO_3$ with a narrow bandgap (3 eV) decreases, the defects in the dielectric layer increase the leakage current and suppress the ultimate dielectric properties. To overcome these limitations caused by the leakage current in Ba-doped $SrTiO_3$, investigations of high-performance capacitors with defect control imparted via interface engineering must be prioritized[6–8].

In this study, the leakage behavior and defect-formation mechanism of a $SrRuO_3/Ba_{0.5}Sr_{0.5}TiO_3/SrRuO_3$ capacitor were investigated through precisely controlled interfacial engineering by using an ultrathin epitaxial scheme to fabricate a 10 nm-thick dielectric layer.

Materials and methods
Thin film growth
All perovskite oxide layers were grown by pulsed laser deposition (PLD) using a KrF excimer laser ($\lambda = 248$ nm). Prior to film growth, a $SrTiO_3$ (100) single-crystal substrate was etched with a buffered hydrofluoric acid etchant and annealed at 1000 °C for 1 h to form a Ti-terminated surface. $SrRuO_3$ and $Ba_{0.5}Sr_{0.5}TiO_3$ perovskite oxides were grown in an oxygen atmosphere at a working pressure of 100 mTorr. During the PLD, the substrate temperature was maintained at 700 °C. The thicknesses of the bottom electrode, dielectric layer, and top electrode were fixed at 30, 10, and 50 nm, respectively. To engineer the interface between the bottom electrode and the dielectric layer, $SrRuO_3$ bottom electrodes were grown with repetition frequencies of 2, 5, and 10 Hz. Subsequently, the $Ba_{0.5}Sr_{0.5}TiO_3$ dielectric layer and $SrRuO_3$ top electrode were grown at an identical frequency of 10 Hz.

Structural and electrical characterization
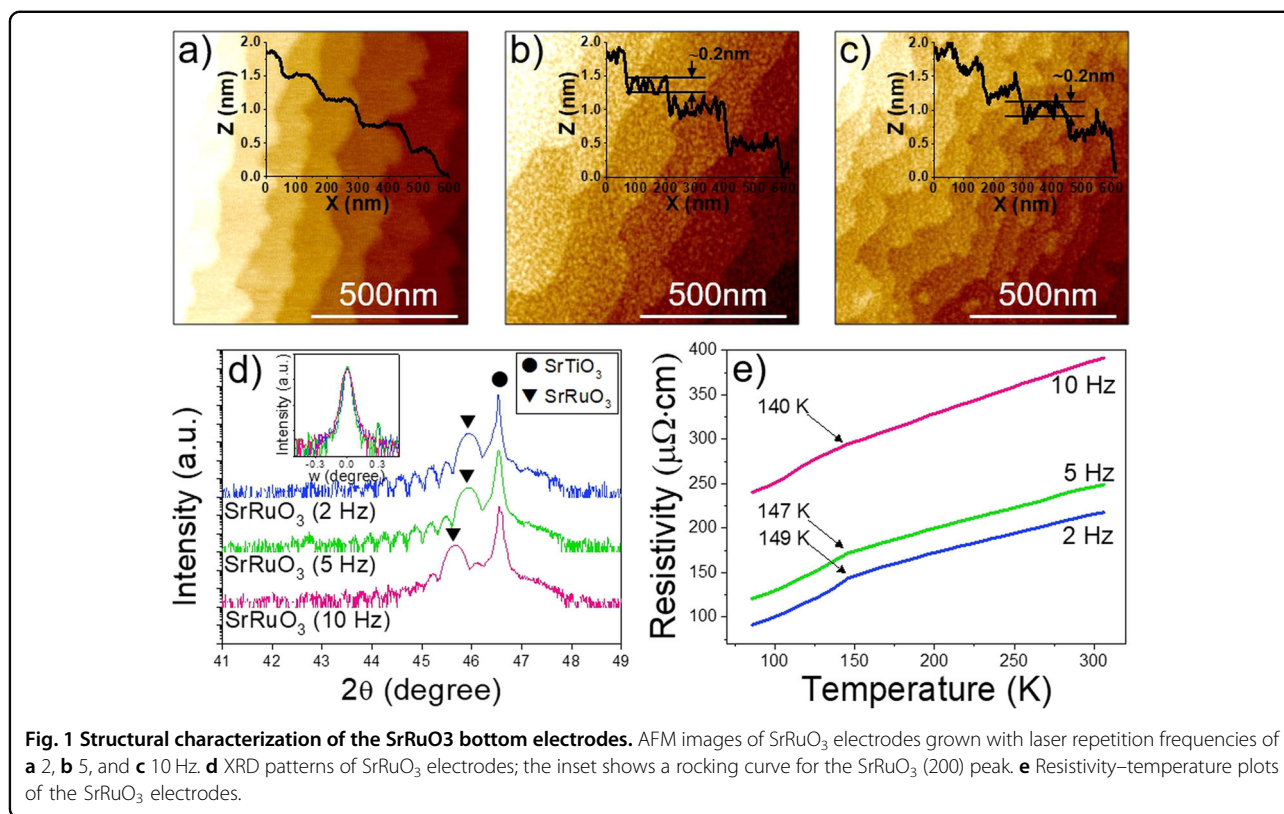AFM, XRD, and the Van der Pauw method were employed to confirm that the $SrRuO_3$ bottom electrodes fabricated at the different repetition frequencies were of high quality. The microstructure of the epitaxially grown $SrRuO_3/Ba_{0.5}Sr_{0.5}TiO_3/SrRuO_3$ capacitor was characterized by cross-sectional HAADF-STEM. The engineered interface between the $SrRuO_3$ bottom electrode and $Ba_{0.5}Sr_{0.5}TiO_3$ was analyzed by HAADF intensity profiling. All of the top $SrRuO_3$ electrodes were defined by patterning with a Ti/Pt hard mask. The temperature-dependent $C-V$ and $I-V$ characteristics were determined using a probe station with a grounded bottom electrode and a biased top electrode.

Band structure predictions
Density functional theory (DFT) calculations were performed with the Vienna Ab Initio simulation package (VASP) based on the projector augmented wave (PAW)[9–12] using the Perdew–Burke–Ernzerhof exchange–correlation functional. The Hubbard-U correction (GGA + U) was applied to more accurately describe the electrons occupying the d orbitals of Ti atoms at the vacant sites. A U value of 4.0 eV was used for Ti atoms[13]. An energy cutoff of 600 eV was used to truncate the plane-wave basis. A $3 \times 3 \times 3$ $SrTiO_3$ supercell with a cubic perovskite structure was studied, and a $3 \times 3 \times 3$ k-point was used following the Monkhorst–Pack scheme. The $SrTiO_3$ supercell was fully relaxed (with a force convergence criterion of 0.001 eV/Å) unless otherwise stated. After structural relaxation, the lattice constant (a) of $SrTiO_3$ was 3.904 Å. Four types of defects were generated in the fully relaxed $SrTiO_3$ supercell. The defects in the four structures were the oxygen vacancy $\left(V_O^{\times}\right)$, Ru substitution $\left(Ru_{Ti}^{\times}\right)$, and two structures in which an oxygen vacancy and Ru substitution coexisted. The two coexistence structures had distances between defects, including distant $\left(\sqrt{1 + 1 + 0.5^2}a = 5.856 \text{ Å}\right)$ and adjacent $\left(\frac{1}{2}a = 1.952 \text{ Å}\right)$ distances. Supercell structures with defects were relaxed under volume fixed conditions. Spin-polarized calculations were performed, and the density of states (DOS) according to the defect type was analyzed.

Results and discussion
A relaxor-ferroelectric $SrRuO_3/Ba_{0.5}Sr_{0.5}TiO_3/SrRuO_3$ capacitor was epitaxially fabricated by PLD. A $Ba_{0.5}Sr_{0.5}TiO_3$ dielectric layer was used for this capacitor to achieve the highest dielectric permittivity based on the dielectric properties of the Ba/Sr ratios (Fig. S1). To control the electrode–dielectric interface, epitaxial $SrRuO_3$ bottom electrodes were grown at different laser repetition frequencies (10, 5, and 2 Hz). Figure 1a–c shows the surface morphologies of these $SrRuO_3$ bottom electrodes, which were imaged by atomic force microscopy (AFM). These results indicated that the $SrRuO_3$ deposited at a repetition frequency of 10 Hz had pits with a half-unit-cell depth (~0.2 nm) on the surface, which did not appear when the repetition frequency was lowered to 2 Hz. These phenomena often occur when epitaxial $SrRuO_3$ films are

Fig. 1 Structural characterization of the SrRuO3 bottom electrodes. AFM images of SrRuO$_3$ electrodes grown with laser repetition frequencies of **a** 2, **b** 5, and **c** 10 Hz. **d** XRD patterns of SrRuO$_3$ electrodes; the inset shows a rocking curve for the SrRuO$_3$ (200) peak. **e** Resistivity–temperature plots of the SrRuO$_3$ electrodes.
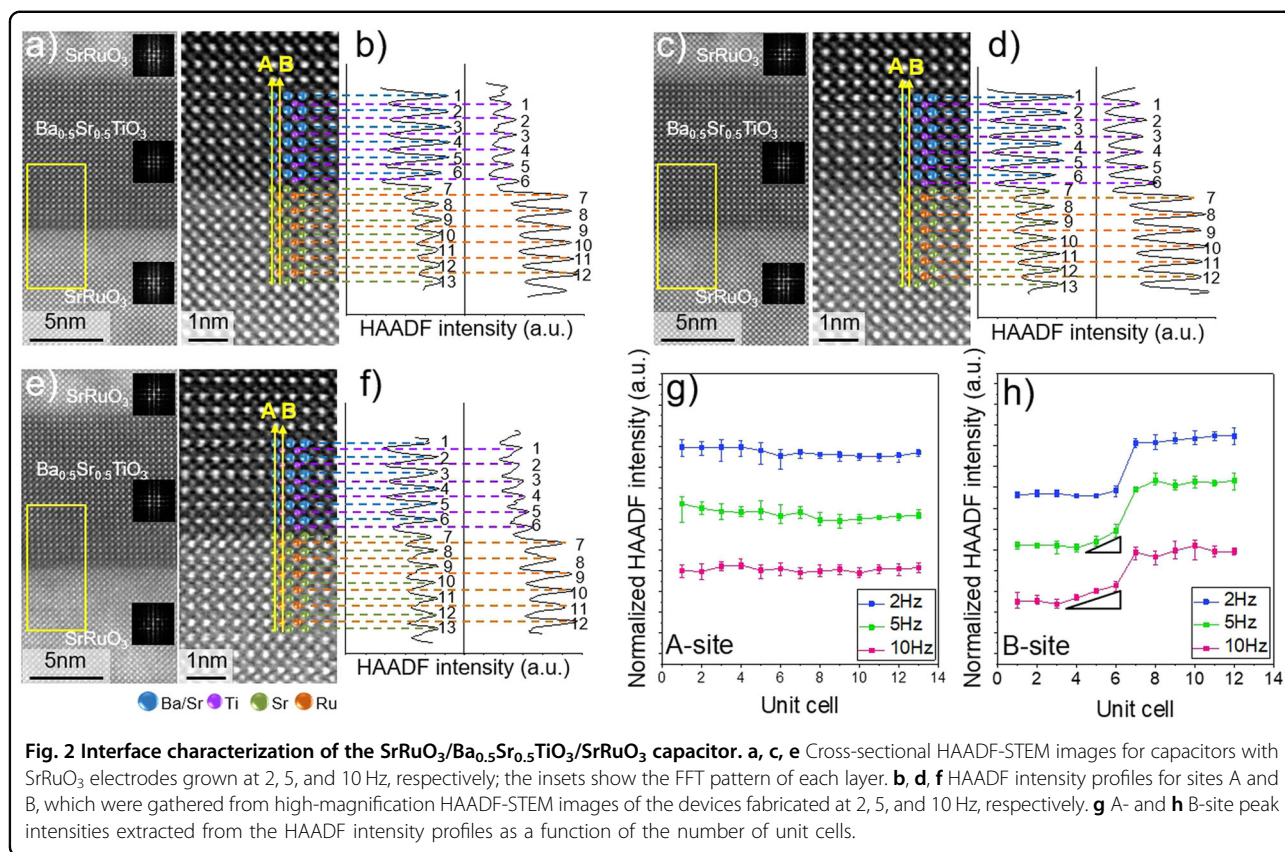
grown by PLD. At high repetition frequencies, each SrRuO$_3$ adatom collides with its adjacent adatom prior to kinetic stabilization of, e.g., the substrate terrace. This collision generates a volatile RuO$_4$ phase and pits on the film surface. Because of these phenomena, epitaxial SrRuO$_3$ films fabricated at high repetition frequencies have Ru-deficient stoichiometries[14]. The Ru/Sr ratios of the SrRuO$_3$ films were determined with respect to the repetition frequency by obtaining Ru-3d core-level X-ray photoelectron spectroscopy (XPS) profiles and comparing them with that of the SrRuO$_3$ target used in growth (Fig. S2). Similarly, the Ru-deficient stoichiometry was estimated by obtaining X-ray diffraction (XRD) patterns and resistivity–temperature data (Fig. 1d, e, respectively). When SrRuO$_3$ has Ru-deficient stoichiometry, it shows an orthorhombic-to-tetragonal phase transition at the critical point. The c-axis of SrRuO$_3$ is consequently lengthened and the XRD peak shifts to lower angles without loss of crystallinity (Fig. 1d)[15–17]. Moreover, Ru-deficient SrRuO$_3$ is known to exhibit a higher resistivity and lower Curie temperature than stoichiometric SrRuO$_3$[18,19]. Therefore, a SrRuO$_3$ bottom electrode with a well-arranged and pit-free surface was obtained at a low PLD repetition frequency for use as the bottom of the electrode–dielectric interface.

To clarify the effects of interface engineering of the MIM capacitor, the Ba$_{0.5}$Sr$_{0.5}$TiO$_3$ dielectric and SrRuO$_3$ top electrodes were grown under identical conditions at the repetition frequencies used for the SrRuO$_3$ bottom electrode. Figure 2a–f shows cross-sectional scanning transmission electron microscopy (STEM) images of the MIM capacitors and the high-angle annular dark-field (HAADF) intensity profiles of the bottom-electrode–dielectric interface with SrRuO$_3$ bottom electrodes fabricated at 2, 5, and 10 Hz, respectively. The peak intensities of the HAADF profiles extracted from sites A and B of the perovskite structure were plotted (Fig. 2g, h). As shown in the cross-sectional STEM and fast Fourier transform (FFT) images (Fig. 2a, c and e), all films were epitaxially grown without any noticeable differences. However, differences were observed for the Ba$_{0.5}$Sr$_{0.5}$TiO$_3$ films with the bottom electrodes in the HAADF intensity profiles of B-site atoms (Fig. 2h). In the case of Ba$_{0.5}$Sr$_{0.5}$TiO$_3$ grown on SrRuO$_3$ at a laser frequency of 10 Hz, the HAADF intensity of the B-site showed a slope with a size of three unit cells; no changes were observed in the A-site intensities. The extent of this slope was decreased to one or two unit cells at the interface between Ba$_{0.5}$Sr$_{0.5}$TiO$_3$ and the bottom SrRuO$_3$ electrode grown at 5 Hz and disappeared at the interface between Ba$_{0.5}$Sr$_{0.5}$TiO$_3$ and the SrRuO$_3$ grown at 2 Hz (Fig. 2g, h). This slope was presumably formed by the half-unit-cell deep pits on the surface of SrRuO$_3$ (Fig. 1a–c). During the growth of Ba$_{0.5}$Sr$_{0.5}$TiO$_3$, interdiffusion can occur

Fig. 2 Interface characterization of the SrRuO₃/Ba₀.₅Sr₀.₅TiO₃/SrRuO₃ capacitor. a, c, e Cross-sectional HAADF-STEM images for capacitors with SrRuO₃ electrodes grown at 2, 5, and 10 Hz, respectively; the insets show the FFT pattern of each layer. **b, d, f** HAADF intensity profiles for sites A and B, which were gathered from high-magnification HAADF-STEM images of the devices fabricated at 2, 5, and 10 Hz, respectively. **g** A- and **h** B-site peak intensities extracted from the HAADF intensity profiles as a function of the number of unit cells.

between pits with high surface energy. Certain atoms from the bottom $SrRuO_3$ layer, especially the B-site Ru, can diffuse to the $Ba_{0.5}Sr_{0.5}TiO_3$ layer.

The dielectric properties of the capacitors were determined based on the repetition frequency used to prepare the $SrRuO_3$ bottom electrodes (Figs. 3 and S4). Although the maximum dielectric permittivity (κ_{max}) value decreased slightly from 931 to 861 as the repetition frequency for preparation of the bottom $SrRuO_3$ electrode was decreased from 10 to 2 Hz, the dissipation factors at both positive and negative voltages were suppressed by more than one order of magnitude (Fig. 3a). Additionally, as the repetition frequency of the bottom $SrRuO_3$ electrode decreased, the leakage current density was dramatically suppressed (Fig. 3b); the leakage current density at a bias of 1 V (J@1 V) decreased from 4.28×10^{-2} to 5.15×10^{-6} A/cm^2.
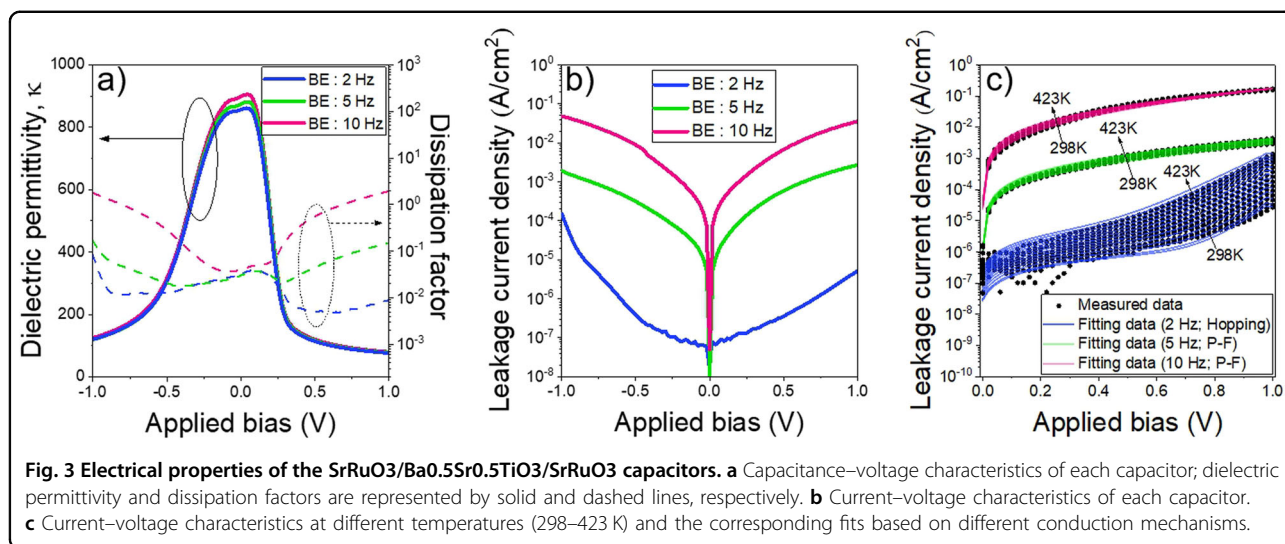
The slight decrease in dielectric permittivity with decreasing laser repetition frequency for fabrication of the bottom electrode can be explained by the HAADF intensity profiles shown in Fig. 2. The effective thickness of $Ba_{0.5}Sr_{0.5}TiO_3$ with 5 and 10 Hz $SrRuO_3$ decreased owing to Ru diffusion at the interface. Therefore, the dielectric permittivity, which was calculated based on the 10 nm-thick $Ba_{0.5}Sr_{0.5}TiO_3$ dielectric layer, increased in proportion to the decrease in the effective thickness of $Ba_{0.5}Sr_{0.5}TiO_3$.

To clarify the four-order-of-magnitude suppression of the leakage current realized via interface engineering, the work functions of $SrRuO_3$ as a function of the repetition frequency were first determined by ultraviolet photoelectron spectroscopy (UPS) to distinguish the material-induced and defect-induced conduction mechanisms (Fig. S3). All of the $SrRuO_3$ films exhibited identical work functions of 5.1 eV, which indicated that material-induced conduction, especially Schottky emission, could be excluded. Next, to reveal the specific mechanism for defect-induced conduction, current–voltage characteristics were determined at different temperatures (Fig. 3c). The obtained fits indicated that hopping conduction occurred in the MIM capacitor with the $SrRuO_3$ grown at 2 Hz, whereas P–F emission occurred in the capacitors with $SrRuO_3$ grown at 5 and 10 Hz. The current density induced by these conduction mechanisms can be expressed with the following equations:

$$J_{hopping} = qan\nu \cdot \exp\left[\frac{qaE}{kT} - \frac{q\varphi_T}{kT}\right], \tag{1}$$

$$J_{P-F} = q\mu N_c E \cdot \exp\left[\frac{-q\left(\varphi_T - \sqrt{qE/\pi\varepsilon_r\varepsilon_0}\right)}{kT}\right], \tag{2}$$

where q is the charge of an electron, a is the hopping distance, n is the electron concentration in the conduction

Fig. 3 Electrical properties of the SrRuO3/Ba0.5Sr0.5TiO3/SrRuO3 capacitors. a Capacitance–voltage characteristics of each capacitor; dielectric permittivity and dissipation factors are represented by solid and dashed lines, respectively. **b** Current–voltage characteristics of each capacitor. **c** Current–voltage characteristics at different temperatures (298–423 K) and the corresponding fits based on different conduction mechanisms.

band, ν is the thermal vibration frequency of electrons at trap sites, E is the applied electrical field, $q\varphi_T$ is the trap energy level, which refers to the activation energy of trapped electrons, μ is the electronic drift mobility, and N_c is the DOS in the conduction band[20]. Using these equations and the data-fitting results, the energy levels of the defects in $Ba_{0.5}Sr_{0.5}TiO_3$ were calculated for the different $SrRuO_3$ growth conditions (Table S1). The shallow defects formed on the rough surfaces of the $SrRuO_3$ bottom electrodes presumably acted as trap sites for P–F emission, indicating that the major defects in the $Ba_{0.5}Sr_{0.5}TiO_3$ dielectric layer can be altered by changing the surface morphology of the bottom electrode.
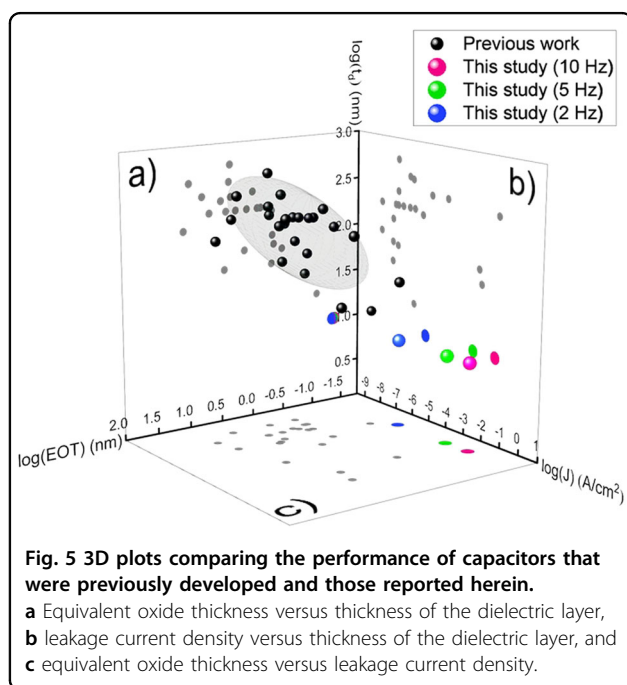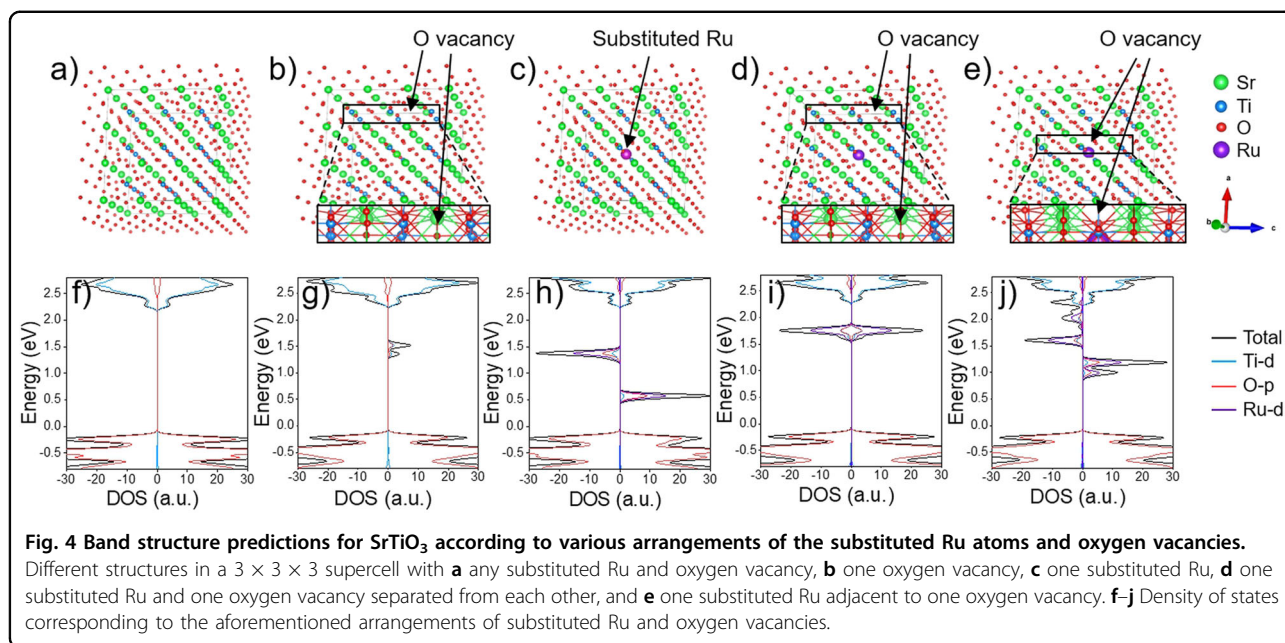
To determine the defects seen at each energy level, DOS data were acquired using $3 \times 3 \times 3$ supercells with five different configurations (Fig. 4f–j). The corresponding structures of the $SrTiO_3$-based supercells were modeled with Ru substitution and oxygen vacancies, and the results are shown in Fig. 4a–e. Ru substitution and oxygen vacancies can be formed by the following reactions:

$$O_O^\times \rightleftharpoons V_O^\times + \frac{1}{2}O_2, \tag{3}$$

$$V_{Ti}^\times + Ru \rightleftharpoons Ru_{Ti}^\times, \tag{4}$$

Ti-$3d$ and O-$2p$ orbitals are known to form the conduction and valance bands in $SrTiO_3$, respectively. Moreover, if oxygen vacancies are present in $SrTiO_3$, two Ti-$3d$ orbitals adjacent to an oxygen vacancy and O-$2p$ orbitals adjacent to each Ti-$3d$ orbital next to the oxygen vacancy form a hybrid orbital, which exhibits in-gap states of 0.7 eV within the bandgap of $SrTiO_3$[21]. The calculation results (Fig. 4f, g) were in good agreement with the observations from these previous studies. If a ruthenium

atom is substituted for a B-site Ti atom, in-gap states are formed that have deep levels similar to those of oxygen vacancies, and these in-gap states consist of Ti-d, O-p, and Ru-d orbitals (Fig. 4h). When a substituted Ru atom and an oxygen vacancy are separated by a significant distance, deep in-gap states are formed in the $SrTiO_3$ bandgap (Fig. 4i). Additionally, if the oxygen vacancy is adjacent to a substituted Ru and the effects of the oxygen vacancy and substituted Ru on changes in the DOS are correlated, a shallow in-gap state is generated just below the conduction band (Fig. 4j). A band diagram including the relative energy states of different defect species is shown in Fig. S5. Therefore, fitting of the data based on the conduction mechanism and the DOS calculation revealed that the orbital interaction between the substituted Ru and oxygen vacancy generated shallow in-gap states, which can act as trap sites for P–F emission in the MIM capacitor containing $SrRuO_3$ electrodes grown with 5- and 10 Hz frequencies.

The electrical properties of the capacitors fabricated in this study were plotted on a 3D graph featuring the following parameters: dielectric film thickness (t_d), equivalent oxide thickness (*EOT*), which is a representative parameter indicating dielectric efficiency based on the thickness of the dielectric layer, and leakage current density (*J*); moreover, these data were compared with those from previous studies (Fig. 5). The electrical properties of previously reported capacitors with $SrRuO_3$ bottom electrodes were specifically compared[22–33]. High-performance capacitors with thinner dielectric layers tend to exhibit lower *EOT* and *J* values. With respect to the *EOT* distribution based on the thickness of the dielectric layer (Fig. 5a), the interface-engineered capacitor with the $SrRuO_3$ bottom electrode grown at 2 Hz exhibited an excellent *EOT* despite having a dielectric layer thinner

Fig. 4 Band structure predictions for SrTiO₃ according to various arrangements of the substituted Ru atoms and oxygen vacancies. Different structures in a 3 × 3 × 3 supercell with **a** any substituted Ru and oxygen vacancy, **b** one oxygen vacancy, **c** one substituted Ru, **d** one substituted Ru and one oxygen vacancy separated from each other, and **e** one substituted Ru adjacent to one oxygen vacancy. **f–j** Density of states corresponding to the aforementioned arrangements of substituted Ru and oxygen vacancies.

Fig. 5 3D plots comparing the performance of capacitors that were previously developed and those reported herein.
a Equivalent oxide thickness versus thickness of the dielectric layer,
b leakage current density versus thickness of the dielectric layer, and
c equivalent oxide thickness versus leakage current density.

than those in previously reported capacitors. Moreover, with respect to the J–t_d distribution (Fig. 5b), the interface engineering performed in this study yielded J values equivalent to those of previously reported capacitors but at a lower dielectric-layer thickness. Additionally, in the EOT–J plot (Fig. 5c), which is typically used to compare the performance of capacitors, the results obtained in this study suggest that a higher performance than those of previously reported devices was achieved.

Conclusions

Interface engineering of epitaxially grown SrRuO₃/Ba₀.₅Sr₀.₅TiO₃/SrRuO₃ capacitors was used to realize a high-performance capacitor containing a thin dielectric layer with high dielectric permittivity and low leakage current. The bottom-electrode/dielectric-layer interface was controlled by using the laser repetition frequency of PLD. A pit-free interface, which was formed by interface engineering at a low laser-repetition frequency, stabilized the Ru atoms in SrRuO₃, which essentially hindered their diffusion from SrRuO₃ to Ba₀.₅Sr₀.₅TiO₃, in contrast to the case for SrRuO₃ with pits on its surface. The interactions between Ru atoms and oxygen vacancies in the dielectric layer are thought to form a shallow in-gap state, which likely acted as the trap site for P–F emission. The engineering of the interface between the bottom SrRuO₃ electrode and Ba₀.₅Sr₀.₅TiO₃ dielectric layer evidently minimized the formation of trap sites and suppressed the leakage current of the capacitor without a large decrease in dielectric permittivity. The estimated dielectric permittivity (861) and leakage current density (5.15×10^{-6} A/cm²) at 1 V for the 10 nm-thick dielectric layer indicated that high dielectric permittivity and low leakage current were achieved simultaneously with the thinnest dielectric layer ever reported. Additionally, this strategy provides clues to facilitating nanoscale integration of DRAM devices.

References

1. Dagdeviren, C. et al. Conformable amplified lead zirconate titanate sensors with enhanced piezoelectric response for cutaneous pressure monitoring. *Nat. Commun.* **5**, 4496 (2014).
2. Damjanovic, D. Ferroelectric, dielectric and piezoelectric properties of ferroelectric thin films and ceramics. *Rep. Prog. Phys.* **61**, 1267 (1998).
3. Ma, W. & Cross, L. E. Flexoelectric polarization of barium strontium titanate in the paraelectric state. *Appl. Phys. Lett.* **81**, 3440–3442 (2002).
4. Jeon, J.-H. Effect of $SrTiO_3$ concentration and sintering temperature on microstructure and dielectric constant of $Ba_{1-x}Sr_xTiO_3$. *J. Eur. Ceram. Soc.* **24**, 1045–1048 (2004).
5. Garten, L. M. et al. Relaxor ferroelectric behavior in barium strontium titanate. *J. Am. Ceram. Soc.* **99**, 1645–1650 (2016).
6. Vehkamäki, M., Hatanpää, T., Hänninen, T., Ritala, M. & Leskelä, M. Growth of $SrTiO_3$ and $BaTiO_3$ thin films by atomic layer deposition. *Electrochem. Solid-State Lett.* **2**, 504 (1999).
7. Kim, S. K. et al. Capacitors with an equivalent oxide thickness of < 0.5 nm for nanoscale electronic semiconductor memory. *Adv. Funct. Mater.* **20**, 2989–3003 (2010).
8. Hou, C. et al. Ultrahigh energy density in $SrTiO_3$ film capacitors. *ACS Appl. Mater. Interfaces.* **9**, 20484–20490 (2017).
9. Kresse, G. & Hafner, J. Ab initio molecular dynamics for liquid metals. *Phys. Rev. B.* **47**, 558 (1993).
10. Kresse, G. & Furthmüller, J. Efficiency of ab-initio total energy calculations for metals and semiconductors using a plane-wave basis set. *Comput. Mater. Sci.* **6**, 15–50 (1996).
11. Kresse, G. & Furthmüller, J. Efficient iterative schemes for ab initio total-energy calculations using a plane-wave basis set. *Phys. Rev. B.* **54**, 11169 (1996).
12. Kresse, G. & Joubert, D. From ultrasoft pseudopotentials to the projector augmented-wave method. *Phys. Rev. B.* **59**, 1758 (1999).
13. Lopez-Bezanilla, A., Ganesh, P. & Littlewood, P. B. Magnetism and metal-insulator transition in oxygen-deficient $SrTiO_3$. *Phys. Rev. B.* **92**, 115112 (2015).
14. Schraknepper, H., Bäumer, C., Gunkel, F., Dittmann, R. & De Souza, R. A. Pulsed laser deposition of $SrRuO_3$ thin-films: the role of the pulse repetition rate. *APL Mater.* **4**, 126109 (2016).
15. Anooz, S. B. et al. Structural and transport properties of $SrRuO_3$ thin films grown by MOCVD on (001) $SrTiO_3$ substrates: the role of built-in strain and extra phases. *Mater. Sci. Eng., B.* **176**, 647–652 (2011).
16. Maria, J. P., Trolier-McKinstry, S., Schlom, D. G., Hawley, M. E. & Brown, G. W. The influence of energetic bombardment on the structure and properties of epitaxial $SrRuO_3$ thin films grown by pulsed laser deposition. *J. Appl. Phys.* **83**, 4373–4379 (1998).
17. Chen, C. L. et al. Epitaxial $SrRuO_3$ thin films on (001) $SrTiO_3$. *Appl. Phys. Lett.* **71**, 1047–1049 (1997).
18. Siemons, W. et al. Dependence of the electronic structure of $SrRuO_3$ and its degree of correlation on cation off-stoichiometry. *Phys. Rev. B.* **76**, 075126 (2007).
19. Lee, S. A. et al. Enhanced electrocatalytic activity *via* phase transitions in strongly correlated $SrRuO_3$ thin films. *Energy Environ. Sci.* **10**, 924–930 (2017).
20. Chiu, F.-C. A review on conduction mechanisms in dielectric films. *Adv. Mater. Sci. Eng.* **2014**, 578168 (2014).
21. Lin, C. & Demkov, A. A. Electron correlation in oxygen vacancy in $SrTiO_3$. *Phys. Rev. Lett.* **111**, 217601 (2013).
22. Pintilie, L., Vrejoiu, I., Hesse, D., LeRhun, G. & Alexe, M. Ferroelectric polarization-leakage current relation in high quality epitaxial Pb(Zr, Ti)O_3 films. *Phys. Rev. B.* **75**, 104103 (2007).
23. Sharma, A. P., Pradhan, D. K., Pradhan, S. K. & Bahoura, M. Large energy storage density performance of epitaxial BCT/BZT heterostructures *via* interface engineering. *Sci. Rep.* **9**, 16809 (2019).
24. Zhang, W. et al. Space-charge dominated epitaxial $BaTiO_3$ heterostructures. *Acta Mater.* **85**, 207–215 (2015).
25. Ventura, J. et al. Structural and dielectric properties of (001) and (111)-oriented $BaZr_{0.2}Ti_{0.8}O_3$ epitaxial thin films. *Thin Solid Films.* **518**, 4692–4695 (2010).
26. Lee, J.-S., Li, Y., Lin, Y., Lee, S. Y. & Jia, Q. X. Hydrogen-induced degradation in epitaxial and polycrystalline (Ba,Sr)TiO_3 thin films. *Appl. Phys. Lett.* **84**, 3825–3827 (2004).
27. Zhu, X., Zheng, D., Peng, W., Miao, J. & Li, J. Structural and electrical properties of epitaxial $Ba_{0.5}Sr_{0.5}TiO_3/SrRuO_3$ heterostructures grown by pulsed laser deposition. *J. Cryst. Growth.* **268**, 192–197 (2004).
28. Abazari, M., Akdoğan, E. K. & Safari, A. Effect of manganese doping on remnant polarization and leakage current in $(K_{0.44}, Na_{0.52}, Li_{0.04})(Nb_{0.84}, Ta_{0.10}, Sb_{0.06})O_3$ epitaxial thin films on $SrTiO_3$. *Appl. Phys. Lett.* **92**, 212903 (2008).
29. Liang, Y.-C. & Liang, Y.-C. Fabrication and electrical properties of strain-modulated epitaxial $Ba_{0.5}Sr_{0.5}TiO_3$ thin-film capacitors. *J. Electrochem. Soc.* **154**, G193 (2007).
30. Acharya, M. et al. Exploring the $Pb_{1-x}Sr_xHfO_3$ system and potential for high capacitive energy storage density and efficiency. *Adv. Mater.* **34**, 2105967 (2022).
31. Gao, D. et al. All-inorganic flexible Ba0.67Sr$_{0.33}$TiO$_3$ thin films with excellent dielectric properties over a wide range of d\frequencies. *ACS Appl. Mater. Interfaces.* **11**, 27088–27097 (2019).
32. Miura, H., Kumagai, Y. & Fujisaki, Y. Hillock growth at the surface of Pt/TiN electrodes for ferroelectric capacitors during annealing in N_2/O_2 ambient. In *MRS Online Proceedings Library (OPL), Volume 493: Symposium U – Ferroelectric Thin Film VI, Materials Research Society* 137 (1997).
33. Dittmann, R. et al. Sharp ferroelectric phase transition in strained single-crystalline $SrRuO_3/Ba_{0.7}Sr_{0.3}TiO_3/SrRuO_3$ capacitors. *Appl. Phys. Lett.* **83**, 5011–5013 (2003).